NAWCWPNS TP 8216

Superspheroid Geometries for Radome Analysis

by
P. L. Overfelt
Research Department

SEPTEMBER 1994

NAVAL AIR WARFARE CENTER WEAPONS DIVISION
CHINA LAKE, CA 93555-6001

Approved for public release; distribution is unlimited.

Naval Air Warfare Center Weapons Division

FOREWORD

This report presents a new body of revolution family of radome contours for high speed missile applications. This research was performed at the Naval Air Warfare Center Weapons Division, China Lake, CA during fiscal year 1994 in support of the C29 Sea Sparrow Upgrade.

This report was reviewed for technical accuracy by David J. White.

Approved by
R. L. DERR, *Head*
Research Department
15 July 1994

Under authority of
D. B. McKinney
RAdm., U.S. Navy
Commander

Released for publication by
S. HAALAND
Deputy Commander for Research and Development

NAWCWPNS Technical Publication 8216

Published by . . . . . Technical Information Department
Collation . . . . . Cover, 17 leaves
First printing . . . . . 80 copies

REPORT DOCUMENTATION PAGE

Form Approved
OMB No. 0704-0188

1. AGENCY USE ONLY *(Leave blank)*	2. REPORT DATE	3. REPORT TYPE AND DATES COVERED
	August 1994	Final Report—January-August 1994

4. TITLE AND SUBTITLE
SUPERSPHEROID GEOMETRIES FOR RADOME ANALYSIS

5. FUNDING NUMBERS
N41756-94-WR 47414

6. AUTHOR(S)
P. L. Overfelt

7. PERFORMING ORGANIZATION NAME(S) AND ADDRESS(ES)
Naval Air Warfare Center Weapons Division
China Lake, CA 93555-6001

8. PERFORMING ORGANIZATION REPORT NUMBER
NAWCWPNS TP 8216

9. SPONSORING/MONITORING AGENCY NAME(S) AND ADDRESS(ES)
Naval Air Warfare Center Weapons Division
China Lake, CA 93555-6001

10. SPONSORING/MONITORING AGENCY REPORT NUMBER

11. SUPPLEMENTARY NOTES

12A. DISTRIBUTION/AVAILABILITY STATEMENT
A Statement; public release; distribution unlimited

12B. DISTRIBUTION CODE

13. ABSTRACT *(Maximum 200 words)*

(U) In the following, we use the arc described by the two-dimensional superquadric equation (taking its exponent, ν, to be any positive real number) in the first quadrant only and revolve it about its major axis to obtain a body of revolution family of geometric shapes called superspheroids. For certain values of length and radius, and assuming that $1 < \nu < 2$, we have determined new shapes that are appropriate for high speed missile radomes. We have found that the superspheroid with optimized exponent value $\nu = 1.381$ can almost exactly reproduce the traditional Von Karman radome geometry. Incidence angle maps and geometric properties have been determined for this superspheroidal family. We have used a ray tracing analysis to obtain boresight error induced by this family of shapes as a function of gimbal angle. The superspheroids are mathematically simple, can approximate most of the traditional radome geometries quite well, and are exceptionally easy to either program or use analytically.

14. SUBJECT TERMS
Radomes, Superspheroids, Superquadrics, Von Karman, Tangent Ogive, Boresight Error

15. NUMBER OF PAGES
34

16. PRICE CODE

17. SECURITY CLASSIFICATION OF REPORT	18. SECURITY CLASSIFICATION OF THIS PAGE	19. SECURITY CLASSIFICATION OF ABSTRACT	20. LIMITATION OF ABSTRACT
UNCLASSIFIED	UNCLASSIFIED	UNCLASSIFIED	UL

CONTENTS

Figures:

CONTENTS (Contd.)

Table:

ACKNOWLEDGMENTS

The author would like to thank Bertha M. Ryan, formerly of DCS Corporation and David J. White of Comarco, Inc., for helpful technical discussion. The author is very grateful to the Naval Sea Systems Command for continued financial support.

I. INTRODUCTION

The two-dimensional superquadric equation (Reference 1)

$$(x/a)^{\nu} + (y/b)^{\nu} = 1 \tag{1}$$

has been applied recently to electromagnetic problems in the context of scattering from perfectly conducting superquadric cylinders (Reference 2) and also in the analysis of reflector antennas with superquadric aperture boundaries (Reference 3). References 2 and 3 have used Equation 1, emphasizing the value of ν to be an integer. However, there is no prohibition against assuming that ν can be any real number, i.e., $\nu \in \mathbf{R}$. Also, generally x and y are assumed to run over the intervals $-a \le x \le a$, $-b \le y \le b$. In the following we write Equation 1 in the form

$$y = (b/a)\,(a^{\nu} - x^{\nu})^{1/\nu} \tag{2}$$

$b \le a$, ν equals any positive real number, and we keep in mind that in taking the ν^{th} root, we are interested in real roots only. In Equation 2 we allow x to take on positive values only, i.e., $0 \le x \le a$. In this case Equation 2 is an arc in the xy-plane, which is completely above the x-axis except at the end point, $x = a$. By taking this arc, $y = f(x) \ge 0$, and revolving it about the x-axis, we obtain a body of revolution (BOR) given by (Reference 4)

$$y^2 + z^2 = (b/a)^2\,(a^{\nu} - x^{\nu})^{2/\nu} \tag{3}$$

having a circular cross section in the yz plane and half of a superquadric cross section in the xz or xy planes. Immediately it is obvious, when $\nu = 2$, that Equation 2 is the arc that will generate the right half of a prolate spheroid. In keeping with previous conventions (Reference 1), we will refer to the BORs generated by Equation 2 when $\nu \neq 2$ as *superspheroids*. We have found that these shapes are quite similar to traditional high speed missile radome shapes when appropriate values of a, b, and ν are used.

For example if we set $z = 0$, $b = 1$, $a = 4$, and $\nu = 1.5$ in Equation 3, in the xy plane we obtain Figure 1, which is a typical radome shape. The parameters b and a can be interpreted as the radome radius and length, respectively. The planar cross section is an open boundary in the xy plane since x is allowed to run between 0 and a only. The radome fineness ratio is given by $a/2\,b$. If some special cases of Equation 3 are considered, we see that when $\nu = 1$, Equation 3 is the equation of a cone (in cross section, a wedge) and when $\nu = 2$, Equation 3 is half of a prolate spheroid (in cross section, half of an ellipse). When $1 < \nu < 2$, we obtain a family of radome cross sections appropriate for high speed missile applications with ν controlling their curvatures (see Figure 2). If blunter nose shapes are desired, one can choose $\nu > 2$, shown in Figure 3, while for pinched shapes, one uses $0 < \nu < 1$, shown in Figure 4. Note that $\nu = 0.2$ produces a mathematical shape that is very close to an aerospike (Reference 5).

The real value of the two-dimensional superquadric Equation 1 or the superspheroidal Equation 3 for radome applications lies in their simplicity. Analytically they are much easier to work with than the Von Karman or ogive equations (Reference 6). Thus since these shapes are mathematically simple, it is possible to obtain closed form expressions for some of the geometric quantities associated with them, such as planar area (Reference 3), volume, etc. Usually this is not possible for traditional radome geometries.

In Section II, we will consider the tangent and normal vectors associated with superspheroids as well as formulas for the curvature and incidence angles since these quantities are necessary for many methods of radome analysis (References 6 through 12). In Section III, we will compare the superspheroid family with traditional radome geometries and show that a number of traditional shapes can be well approximated by superspheroids using appropriate values for a, b, and ν. In Section IV, we will indicate how to determine the arc length, area, and volume properties of such shapes. In Section V, we use a ray tracing technique to obtain boresight error curves as functions of gimbal angle for various superspheroid geometries and compare the electrical properties of a Von Karman shape and an optimized superspheroid. Section VI contains our conclusions.

II. TANGENTS, NORMALS, AND INCIDENCE ANGLE MAPS

Considering the arc in the first quadrant of the xy plane where $y = f(x) \geq 0$ for $0 \leq x \leq a$, we find that the derivative of Equation 2 is simply

$$f'(x) = -\frac{b}{a} x^{\nu-1} \left(a^{\nu} - x^{\nu}\right)^{\left(\frac{1}{\nu}-1\right)} \quad . \tag{4}$$

Setting the antenna gimbal point at the coordinate origin, the equation of the central ray projected from the origin is just

$$y = x \tan \psi \tag{5}$$

where ψ is the antenna gimbal angle.

The x-coordinate of the point at which the central ray (or radius vector) intersects the superquadric is given by

$$x_i = \frac{ab}{\left[a^{\nu}(\tan \psi)^{\nu} + b^{\nu}\right]^{1/\nu}} \quad . \tag{6}$$

The unit tangent vector to the superquadric is

$$\hat{t} = \frac{a\left(a^{\nu} - x^{\nu}\right)^{1-\frac{1}{\nu}} \hat{x} - bx^{\nu-1} \hat{y}}{\left\{a^2\left(a^{\nu} - x^{\nu}\right)^{2-\frac{2}{\nu}} + b^2 x^{2(\nu-1)}\right\}^{1/2}} \tag{7}$$

and the unit normal is

$$\hat{n} = \frac{bx^{\nu-1} \hat{x} + a\left(a^{\nu} - x^{\nu}\right)^{1-\frac{1}{\nu}} \hat{y}}{\left\{a^2\left(a^{\nu} - x^{\nu}\right)^{2-\frac{2}{\nu}} + b^2 x^{2(\nu-1)}\right\}^{1/2}} \quad . \tag{8}$$

Thus the incidence angle, θ, is given by either

$$\cos \theta = \left(\hat{r} \bullet \hat{n}\right) \tag{9}$$

or

$$\sin\theta = \left(\hat{r} \bullet \hat{t}\right) \tag{9a}$$

where the unit radius vector, $\hat{r}$ has been written in the form

$$\hat{r} = \frac{\hat{x} + \tan\psi\,\hat{y}}{\sqrt{1+\tan^2\psi}} \quad . \tag{10}$$

Dividing Equation 9a by Equation 9 and substituting Equation 6 into $\hat{n}$ and $\hat{t}$, we obtain a convenient form for the incidence angles of superspheroid shapes in the *xy* plane as a function of the antenna gimbal angle, i.e.,

$$\tan\theta = \frac{\left[a^{2\nu}(\tan\psi)^{\nu}\right]^{\left(1-\frac{1}{\nu}\right)} - b^{\nu}a^{\nu-2}\tan\psi}{\tan\psi\left[a^{2\nu}(\tan\psi)^{\nu}\right]^{\left(1-\frac{1}{\nu}\right)} + b^{\nu}a^{\nu-2}} \quad . \tag{11}$$

Note that for $\nu = 2$, i.e., half of an ellipse, Equation 11 reduces to

$$\tan\theta = \frac{a^2 - b^2}{a^2\tan\psi + b^2 ctn\psi} \tag{12}$$

as given in Reference 6. Plotting Equation 11, Figures 5 through 8 show incidence angle maps for given fineness ratios and different values of ν.

In some radome analysis methods, attempts have been made to take curvature directly into account (References 13 and 14). In such methods, it is often helpful to know the principal radii of curvature. The first and second principal radii of curvature are given by the standard formulas (References 15 and 16)

$$R_1 = \frac{\left[1+f'(x)^2\right]^{3/2}}{f''(x)} \quad , \quad R_2 = -f(x)\left[1+f'(x)^2\right]^{1/2} \tag{13}$$

or for the superspheroids

$$R_1 = \frac{\left\{ a^{1-\nu} x^{2-\nu} \left(a^\nu - x^\nu\right)^{\left(2-\frac{1}{\nu}\right)} \left[1 + \left(\frac{b}{a}\right)^2 x^{2(\nu-1)} \left(a^\nu - x^\nu\right)^{\left(\frac{2}{\nu}-2\right)} \right]^{\frac{3}{2}} \right\}}{b(1-\nu)} \tag{14}$$

while

$$R_2 = -\frac{b}{a}\left(a^\nu - x^\nu\right)^{1/\nu} \left[1 + \left(\frac{b}{a}\right)^2 x^{2(\nu-1)} \left(a^\nu - x^\nu\right)^{\left(\frac{2}{\nu}-2\right)} \right]^{1/2} . \tag{15}$$

When the value of ν is 2, the formulas for R_1 and R_2 reduce to those for a spheroidal surface given in Reference 15.

Also, the superspheroids possess the quality of similarity (Reference 17), meaning that one can obtain curves from the superspheroid equation that are exactly the same in form and that differ only in scale. For example a simple generalization of Equation 1 in the xy plane is

$$\left(\frac{x}{a}\right)^\nu + \left(\frac{y}{b}\right)^\nu = \eta \tag{16}$$

where η is any constant. This automatically causes the a and b parameters to scale to

$$\frac{x^\nu}{\eta a^\nu} + \frac{y^\nu}{\eta b^\nu} = 1 \tag{17}$$

or the new a and b are $a' = a\eta^{1/\nu}$, $b' = b\eta^{1/\nu}$. Thus we can use Equation 16 to obtain "nested" or similar superquadrics where the fineness ratio of each shape is $\frac{a}{2b} = \frac{a'}{2b'}$ and is independent of η (see Figure 9). This quality is not always present (or, if present, is not always obvious) in the equations describing traditional radome geometries.

III. APPROXIMATION OF TRADITIONAL RADOME SHAPES USING SUPERSPHEROIDS

In this section, we compare the equations describing the Von Karman, Sears-Haack, tangent ogive, and power law radomes with superspheroidal approximations. Beginning with the Von Karman geometry, we use the Haack-Von Karman equation in the xy plane (References 6 through 8),

$$y^2 = \frac{D^2}{4\pi}\left[\zeta - \frac{1}{2}\sin 2\zeta + \kappa \sin^3 \zeta\right] \tag{18}$$

where

$$\zeta = \cos^{-1}\left(\frac{2(x+h)}{\ell} - 1\right) \tag{19}$$

and

κ = a constant
D = diameter
ℓ = total length
h = antenna gimbal point of the radome.

When the constant κ is equal to zero, we have a Von Karman shape. When κ is equal to one-third, we have a Sears-Haack shape. Both of these geometries have been very successful in radome design due mainly to their aerodynamic properties (Reference 6).

In attempting to approximate the traditional radome shapes with superspheroids, we have used the distance between two curves, $f(x)$ and $g(x)$, given by (Reference 18)

$$\|f-g\| = \left\{\int_0^a [f(x)-g(x)]^2\, dx\right\}^{1/2} \tag{20}$$

as a measure of how "good" the approximation is. Equation 20 is a functional of the least-squares type and is the simplest possible functional, which yields an accurate positive definite residual (Reference 19). Thus by minimizing ||f-g||, and choosing fixed values for a and b, we can find that value of ν, which corresponds to the minimum of ||f-g||. This value of ν is then optimum in providing the "best" approximation of $g(x)$ to $f(x)$ in the

least-squares sense. Table 1 gives the optimized values of ν, which result in the best least-squares approximation of the superspheroid geometry to the Von Karman, tangent ogive, Sears-Haack and power law radome contours. The optimum value of ν is not affected by changes in the radome fineness ratio.

Table 1. Optimized Values of ν.

Shape	Optimum ν	Minimum ‖f-g‖
Von Karman	1.381	0.00915
Tangent Ogive	1.449	0.06756
Sears-Haack	1.555	0.02523
Power Law ($m = \frac{3}{4}$)	1.161	0.03012
Power Law ($m = \frac{1}{2}$)	1.457	0.067711
Power Law ($m = \frac{1}{4}$)	2.252	0.104671

Figure 10a shows a comparison between a Von Karman shape with D = 2, ℓ = 4, h = 0, κ = 0, and a superspheroid with a = 4, b = 1, ν = 1.381. We have found that these two geometries are indistinguishable graphically over a range of ν where $1.34 < \nu < 1.40$. Thus the approximation of the Von Karman by a superspheroid is not very sensitive to changes in the ν parameter. When κ is equal to one-third, Equation 18 describes a Sears-Haack radome shape. Figure 10b shows a comparis on between the Sears-Haack geometry with D = 2, ℓ = 4, h = 0, and a superspheroid with b = 1, a = 4, ν = 1.555. As for the Von Karman shape, the difference between the superspheroid and Sears-Haack is indistinguishable graphically.

Comparison between a tangent ogive and a superspheroid is shown in Figure 10c. The ogive defining equation in the xy plane is

$$y^2 = \left(\sqrt{R^2 - x^2} + b_a - R\right)^2 \tag{21}$$

where b_a = base radius and R = radius of the "parent circle," which traces out the shape. The tangent ogive is much harder to approximate using a superspheroid than the Von Karman or Sears-Haack shapes.

In Figure 10c, we have chosen b_a = 1, R = 8.5 for the tangent ogive, and a = 4, b = 1, and ν = 1.449 for the approximating superspheroid. This value of ν causes the two geometries to match in an overall sense but with significant differences near x = 1 and $3 \leq x \leq 4$. It it not surprising that the comparison between the tangent ogive and the superspheroid is worse than for the Von Karman; since at the nose the derivatives of the two shapes are fundamentally different with the tangent ogive having no unique derivative at x = a while the superspheroid derivative is infinite there when $\nu > 1$. However for many numerical purposes, the approximation of a tangent ogive by a superspheroid (with ν = 1.449) would be acceptable.

The set of previously known shapes which is closest analytically to the superspheroids is the set of power law shapes (Reference 6). They are defined in the xy plane by

$$y = \frac{D}{2}\left(\frac{\ell - x}{\ell}\right)^m \tag{22}$$

where

D = base diameter
ℓ = length
m = constant.

In its three-dimensional form, when m is one-half we obtain a paraboloid, and when m is one, Equation 22 defines a cone. The most famous of this set of shapes is the three-quarter power law (m = 0.75) which is itself an approximation to a true Newtonian shape.

Figure 10d compares the three-quarter power law shape with a superspheroid where D = 2, ℓ = 4, m = 0.75, and a = 4, b = 1, ν = 1.161. As for the Von Karman and Sears-Haack contours, the three-quarter power law shape and the optimum superspheroid are again graphically indistinguishable. However as shown in Figure 11a and 11b, as m decreases to one-half and further to one-fourth, it is much harder to approximate the power law shapes using optimized superspheroids. While the power law shapes are analytically as simple as the superspheroids, they are unable to approximate the Von Karman, Sears-Haack, or tangent ogive geometries as well as do the superspheroid family.

IV. GEOMETRIC PROPERTIES

Now we consider the planar area, volume, arc length, and lateral area of the surface of revolution of the superspheroids. The planar area of the superspheroids (in the xy plane) is given by the area between the two arcs, $y = \pm f(x)$, such that

$$A = \frac{2b}{a}\int_0^a \left(a^\nu - x^\nu\right)^{1/\nu} dx \quad . \tag{23}$$

Equation 23 can be evaluated in closed form using gamma functions and is given by

$$A = \frac{2ab}{\nu}\frac{\Gamma\left(1+\frac{1}{\nu}\right)\Gamma\left(\frac{1}{\nu}\right)}{\Gamma\left(1+\frac{2}{\nu}\right)} \quad ; \quad \nu > 0 \quad . \tag{24}$$

The planar area for superquadrics with closed boundaries (i.e., $-a \le x \le a$, $-b \le y \le b$) was given in a somewhat different form in Reference 3.

Considering some special cases of Equation 24, when $\nu = 1$, we have $A = ab$, the plane area of a wedge; when $\nu = 2$, $A = \frac{\pi ab}{2}$, the area of half an ellipse; and as $\nu \to \infty$, $A \to 2ab$, the area of a rectangle in the right half plane only.

The volume of the superspheroids is given by the integral

$$V = \pi b^2 \int_0^a \left[1 - \left(\frac{x}{a}\right)^\nu\right]^{2/\nu} dx \quad . \tag{25}$$

Equation 25 can be evaluated in closed form also, using the variable substitution $t = \left(\frac{x}{a}\right)^\nu$, resulting in

$$V = \frac{\pi b^2 a}{\nu} \frac{\Gamma\left(1+\frac{2}{\nu}\right)\Gamma\left(\frac{1}{\nu}\right)}{\Gamma\left(1+\frac{3}{\nu}\right)} \quad ; \quad \nu > 0 \quad . \tag{26}$$

Again considering some special cases of Equation 26, when $\nu = 1$, $V = \frac{1}{3}\pi b^2 a$, which is the volume of a cone with base radius b and altitude a. When $\nu = 2$, $V = \frac{2\pi b^2 a}{3}$, which is the volume of half of a prolate spheroid. When $\nu \rightarrow \infty$, the superspheroid geometry becomes that of a circular cylinder with length a and radius b and volume $\pi b^2 a$. Thus by normalizing the superspheroid for any ν to $\pi b^2 a$, we obtain Figure 12, which shows normalized volume as a function of ν. The top (Figure 12a) is a blow-up of the region $0 < \nu < 2$ while the bottom (Figure 12b) shows the volume behavior when ν is large. It is interesting that as ν becomes less than 0.4, the volume decreases sharply toward zero.

The arc length of the superspheroids is a far more difficult property to determine analytically. We have found that the arc length can be put in the form of a generalization of the complete elliptic integral of the second kind, i.e. the arc length is

$$L = \frac{4a}{\nu} \int_0^1 \left[\frac{\left(1-t^2\right)^p + k^2 t^{(2p)}}{\left(1-t^2\right)^p} \right]^{1/2} t^{(1-p)} dt \tag{27}$$

where $t = \left(\frac{x}{a}\right)^{\nu}$, $p = 2 - \frac{2}{\nu}$, and $k = \frac{b}{a}$. Immediately for the case of the ellipse ($\nu = 2$), we have $p = 1$ and Equation 27 reduces to

$$L = 2a \int_0^1 \left[\frac{\left(1-t^2 k'^2\right)}{1-t^2} \right]^{1/2} dt \tag{28}$$

where

$$k'^2 = 1 - k^2 = 1 - \left(\frac{b}{a}\right)^2$$

or

$$L = 2aE(k') \tag{29}$$

where E(k') is the complete elliptic integral of the second kind (Reference 20).

For the cone, where $\nu = 1$ and $p = 0$, Equation 27 becomes $L = a\sqrt{1+\left(\frac{b}{a}\right)^2}$. In Figure 13, we have plotted the arc length normalized to 2a versus ν for various fineness ratios, $\frac{a}{2b} = 1$, 2, and 3. These curves are quite similar in appearance, each sharing a minimum at $\nu = 1$. This, of course, indicates that the arc length of the cone is the minimum of all the superspheroidal shapes. As $\nu \to \infty$, the arc length of the superspheroids plane goes to that of a rectangle of perimeter $L \to 2(a+b)$. Thus $\frac{L}{2a} \to 1 + \frac{b}{a}$, and we see in Figure 13, that for ν large, $1 + \frac{b}{a}$ is the asymptotic limit for each curve and as $\nu \to 0$, $1 + \frac{b}{a}$ is the limit for each curve also. Thus no matter how small ν becomes, the arc length does not approach zero even though the volume does.

The lateral surface area of the superspheroids is determined similarly. We have found that this quantity is given by

$$S = \frac{4\pi ab}{\nu}\int_0^1 \left[\left(1-t^2\right)^p\left(t^2\right)^{p-2} + k^2\left(1-t^2\right)^{2p-2}\right]^{1/2} t\,dt \tag{30}$$

where

$$t = \left(\frac{x}{a}\right)^{\nu}$$

$$p = \frac{2}{\nu}$$

$$k = \frac{b}{a}\ .$$

From Equation 30, we find that the lateral surface area of a cone ($\nu = 1$) is $S_{cone} = \pi b\sqrt{a^2+b^2}$ while the lateral surface area of half of a spheroid is

$$S_S = \pi b^2 + \pi ab \frac{\sin^{-1}(k')}{k'} \tag{31}$$

where $k' = \sqrt{1-\left(\frac{b}{a}\right)^2}$. In Figure 14, we have plotted the lateral surface area in Equation 30 normalized to the lateral surface area of a circular cylinder versus ν for the same fineness ratios as in Figure 13, i.e., $\frac{a}{2b} = 1, 2, 3$. These curves approach one as ν gets very large (the area approaches the lateral area of the circular cylinder, $2\pi ab$). As $\nu \rightarrow 0$, each curve approaches a nonzero limit, $\frac{b}{2a}$.

V. NUMERICAL COMPARISON OF ELECTRICAL PARAMETERS USING RAY TRACING

Using a ray tracing computer program developed at the Naval Air Warfare Center Weapons Division, China Lake, CA (Reference 7), we can compare the electrical performance of a Von Karman radome with that of the corresponding optimized superspheroid with $\nu = 1.381$. Also we can evaluate the performance of the superspheroid family of contours in terms of boresight error (BSE), boresight error slope (BSES), and power transmission. Throughout we assume that the antenna is linearly polarized along the y axis such that the elevation plane corresponds to what is generally called the E-plane and the azimuth plane corresponds to the H-plane. Initially we have assumed a single layer radome of wall thickness $\lambda/2$ at 10 GHz and $\epsilon = 5.5$ (pyroceram), a two to one fineness ratio, and an antenna aperture of 6 inches.

In Figures 15 through 20, each of the parameters characterizing the radome and the antenna is varied, and the effect of this variance on BSE, BSES, and power transmission is determined. Figure 15a compares the BSE in both elevation and azimuth planes from a Von Karman radome with that from the optimized superspheroid as a function of antenna gimbal angle. Figure 15b compares their BSES and Figure 15c compares their power transmission. There are small discrepancies in the BSE from the two contours in both planes, but the general agreement is close as would be expected from the closeness of the geometric approximation. The elevation BSE shows worse agreement near the nose region and better agreement beyond the 15-degree gimbal angle; while this effect is exactly the opposite in the azimuth plane. The same is true of the error slope and the power transmission. There are small differences in each case, but, in general the differences between the Von Karman and the superspheroid shapes are negligible in terms of the limits of accuracy of the ray tracing method.

In Figure 16, the fineness ratio of the two shapes has been increased to 3 to 1. Figure 16a compares the elevation and azimuth BSE, Figure 16b compares the error slopes in both planes, and Figure 16c compares the power transmission in both planes. Increasing to this larger fineness ratio either has no effect on the curves or causes them to have better agreement. Figure 17a, b, and compare the two shapes when their fineness ratio is decreased to 1.5 to 1. All the electrical parameters still agree very closely and we conclude that a change in fineness ratio does not affect the electrical characteristics.

In Figure 18, we consider the effect of changing the antenna aperture size on the electrical properties of the Von Karman and superspheroid contours. BSE is shown in Figure 18a, BSES in Figure 19b, and transmission in Figure 19c for both principal planes. Again little effect is noted.

If the geometric size, the radome wall thickness, and the dielectric constant remain the same while the frequency is increased, the wall will be much thicker electrically; causing larger BSE, BSES, and transmission loss. Figures 19a, b, and c show the effect of increasing the frequency from 10 to 13 GHz. In this case the difference between the electrical performance of the Von Karman and superspheroid contours is larger for BSE, BSES, and power transmission. Thus changing to an electrically thicker wall is a situation that causes distinct differences in the respective electrical performance of the two shapes.

Finally in Figures 20a, b, and c, we have considered the effect of multiple layers on the comparison between the Von Karman and superspheroid shapes. Using a symmetric A-sandwich wall, we find that there is close agreement between BSE, BSES, and transmission curves in both principal planes.

Figures 21a and b indicate the BSE behavior of the superspheroids as a function of gimbal angle for various ν values. For a 2 to 1 fineness ratio and $1.2 < \nu < 2.0$, we see that typical BSE curves result for both the elevation plane in Figure 21a and the azimuth plane in Figure 21b. In the elevation plane the smallest BSE occurs at $\nu = 1.2$, the largest at $\nu = 2.0$. In the azimuth plane the smallest BSE occurs at $\nu = 1.4$, the largest at $\nu = 2.0$. Thus for this particular case, a more conical radome produces less BSE (in the elevation plane) than a more elliptically shaped radome. In the azimuth plane a more intermediate shape produces less BSE for this case.

VI. CONCLUSIONS

We have used the two-dimensional superquadric equation in the first quadrant and revolved it about its major axis to obtain a body of revolution family of geometric shapes called superspheroids. For certain values of length and radius and assuming that $1 < \nu < 2$, we have determined shapes appropriate for high speed missile radomes. We have found that the superspheroid characterized by the curvature parameter $\nu = 1.381$ is an almost exact match for the Von Karman shape. We have determined incidence angle maps, geometric properties, and used ray tracing to obtain boresight error as a function of gimbal angle for

the superspheroids. This family of shapes is mathematically simple, can approximate most of the traditional radome geometries quite well, and is exceptionally easy to either program or use analytically.

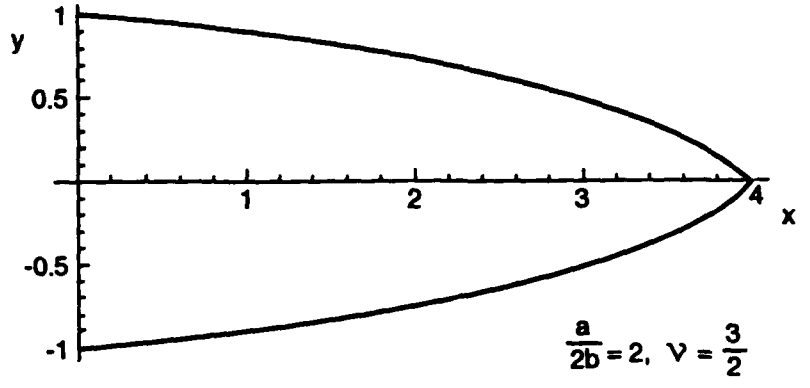

FIGURE 1. Superspheroid Cross Section in the xy Plane ($z = 0$, $b = 1$, $a = 4$, $\nu = 1.5$).

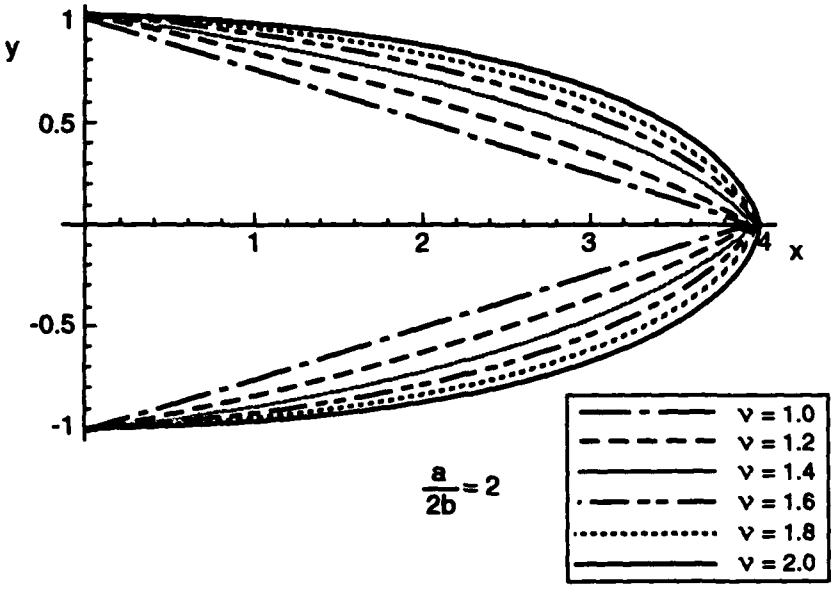

FIGURE 2. Family of Superspheroid Cross Sections in the xy Plane ($z = 0$, $b = 1$, $a = 4$, $1 \leq \nu \leq 2$).

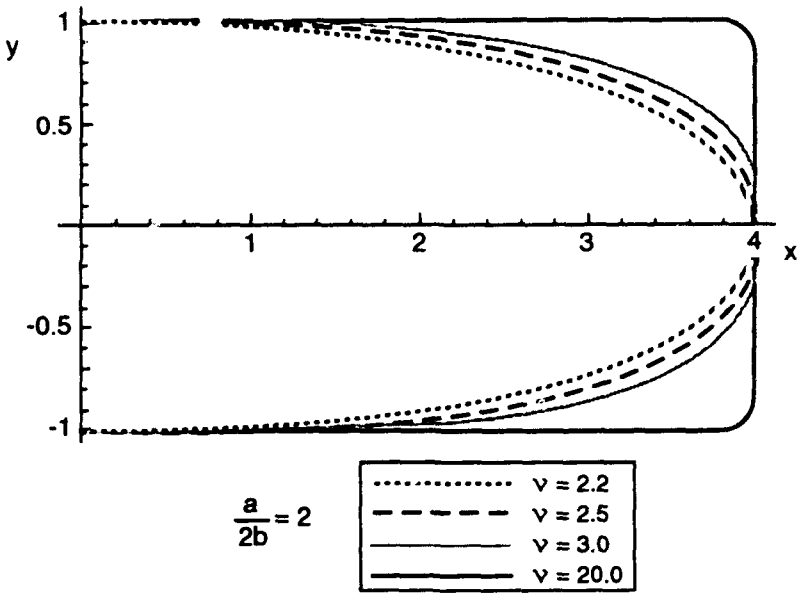

FIGURE 3. Family of Superspheroid Cross Sections in the xy Plane ($z = 0, b = 1, a = 4, \nu > 2$).

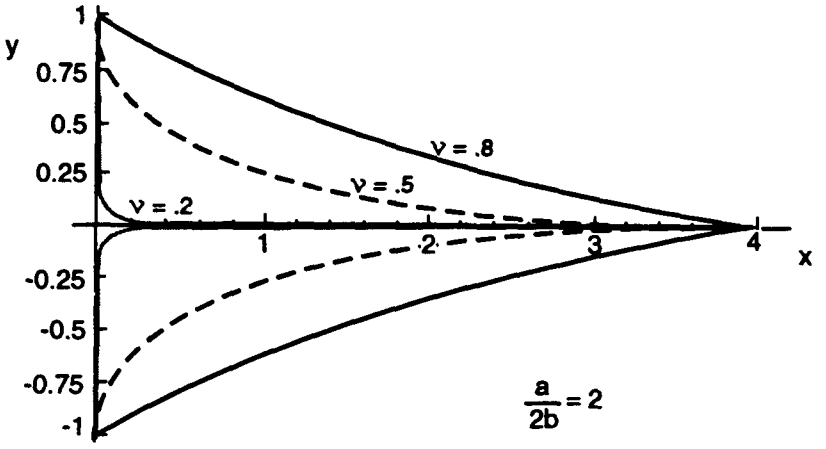

FIGURE 4. Family of Superspheroid Cross Sections in the xy Plane ($z = 0, b = 1, a = 4, 0 < \nu < 1$).

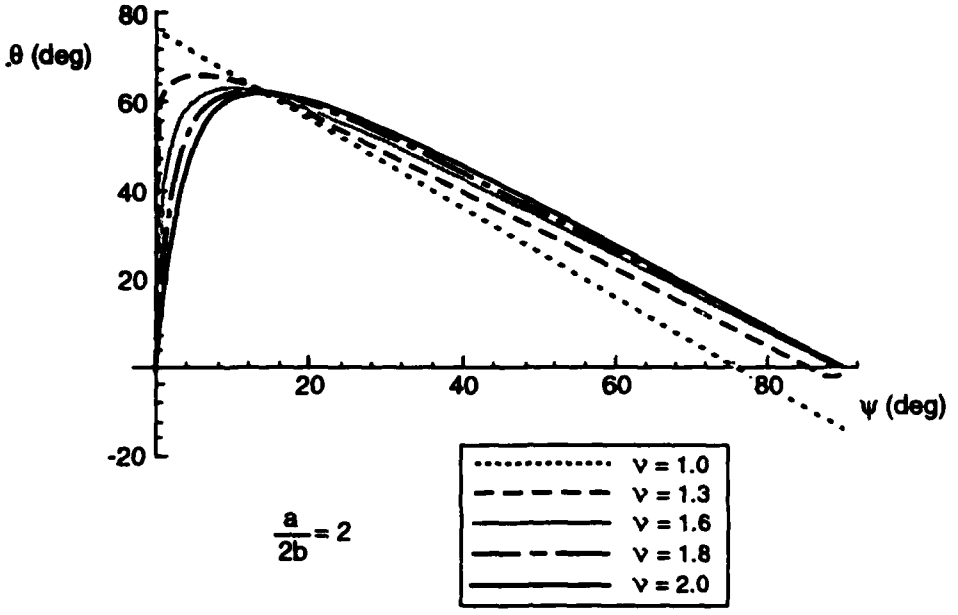

FIGURE 5. Superspheroid Incidence Angle Map for a 2-1 Geometry Using ν as a Parameter ($1 \leq \nu \leq 2$).

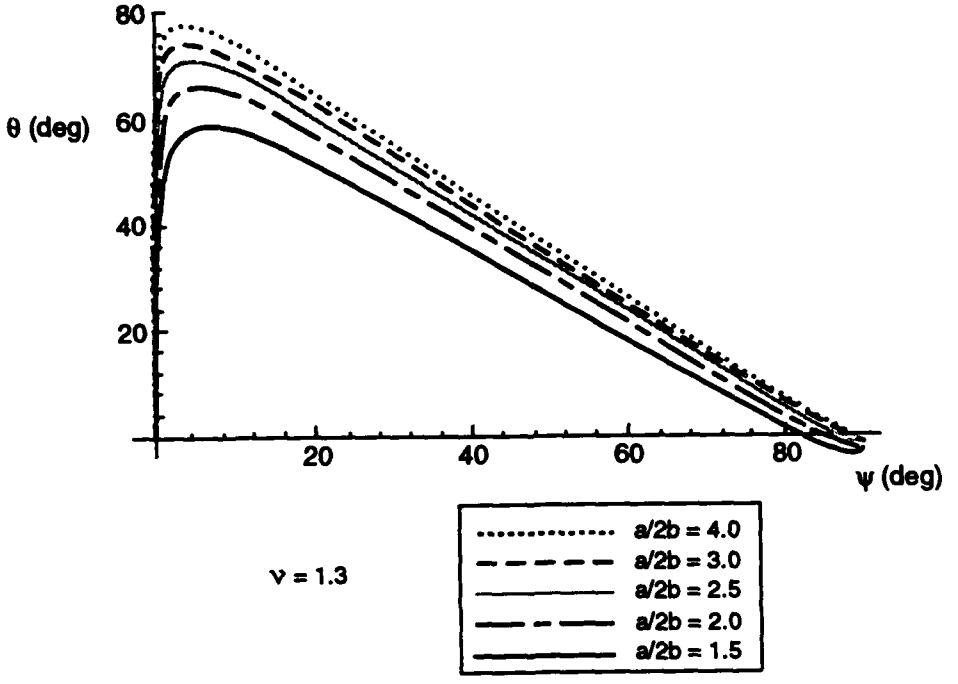

FIGURE 6. Superspheroid Incidence Angle Map for ν = 1.3, Using the Fineness Ratio as a Parameter.

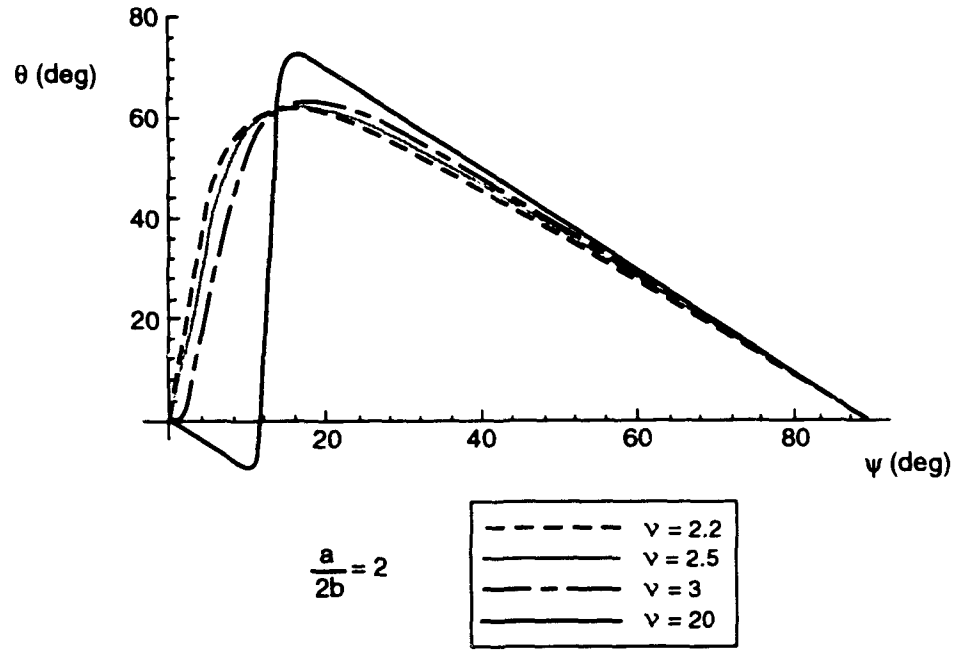

FIGURE 7. Superspheroid Incidence Angle Map for a 2-1 Geometry Using ν as a Parameter (ν > 2).

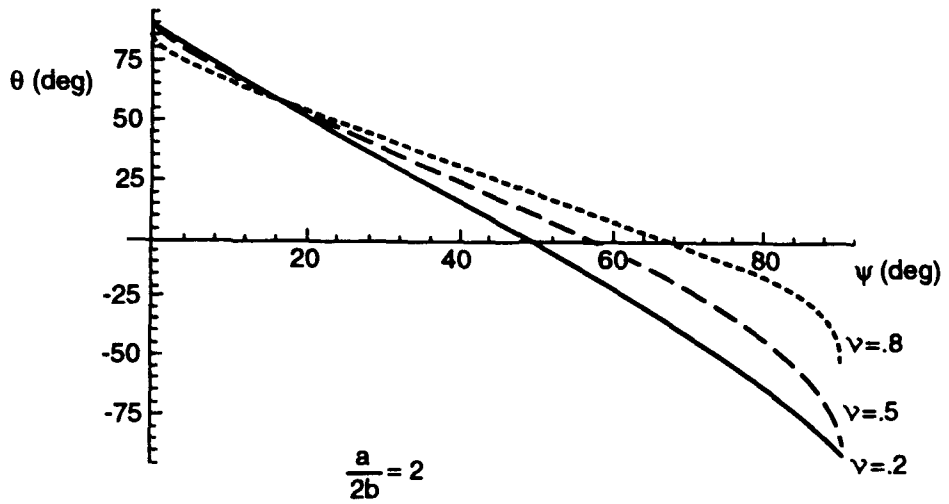

FIGURE 8. Superspheroid Incidence Angle Map for a 2-1 Geometry Using ν as a Parameter (0 < ν < 1).

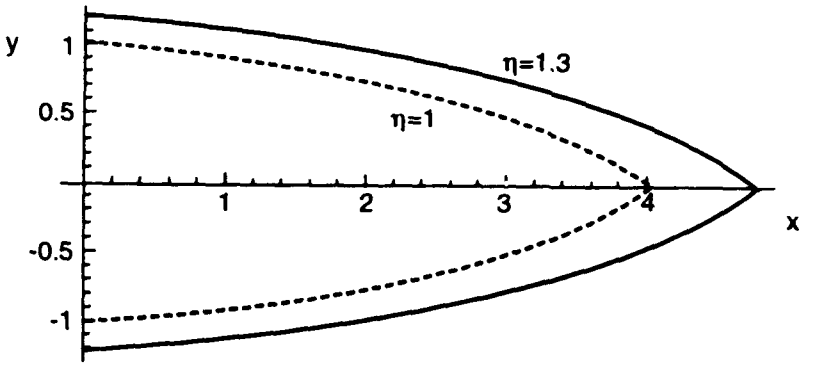

FIGURE 9. "Nested" Superspheroid Cross Sections in the *xy* Plane With η = 1.0 and 1.3.

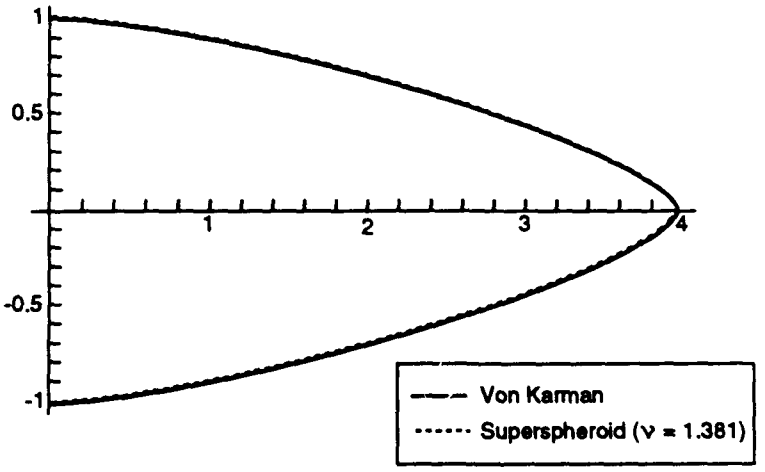

(a). Comparison between a Von Karman and a superspheroid geometry (D = 2, ℓ = 4, h = 0; a = 4, b = 1, ν = 1.381).

FIGURE 10. Comparison of a Superspheroid Geometry With a Von Karman, a Sears-Haack, Tangent Ogive, and Three-Quarter Power Law Geometry.

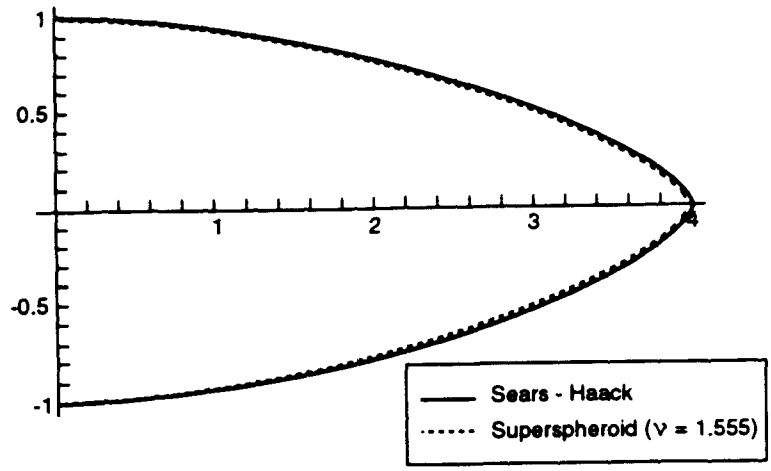

(b). Comparison between a Sears-Haack and a superspheroid geometry (D = 2, ℓ = 4, h = 0, $\kappa = \frac{1}{3}$; a = 4, b = 1, ν = 1.555).

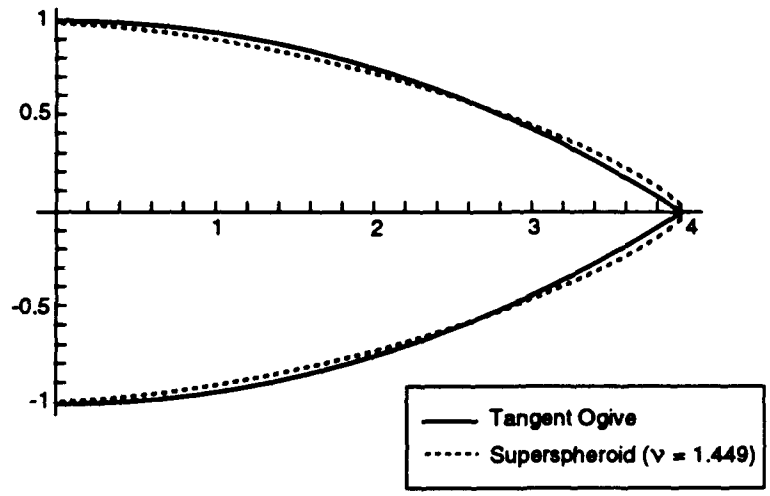

(c). Comparison between a tangent ogive and a superspheroid geometry (b_a = 1, R = 8.5; a = 4, b = 1, ν = 1.449).

FIGURE 10. (Contd.)

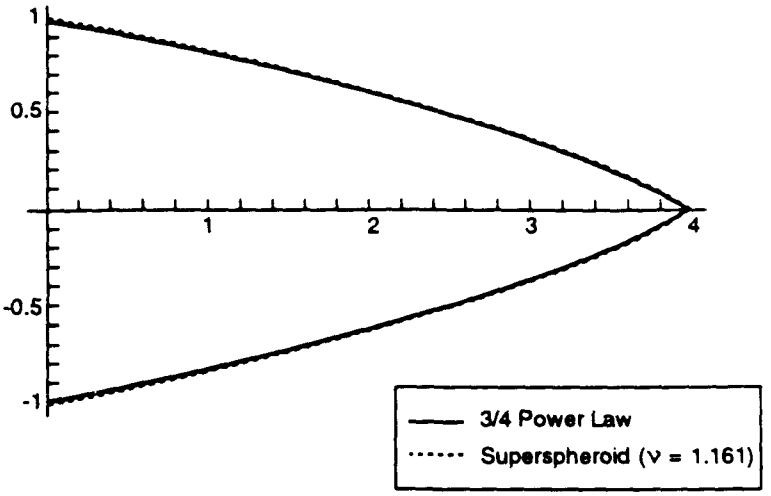

(d). Comparison of a three-quarter power law and a superspheroid (D= 2, ℓ = 4, m = 0.75; a = 4, b = 1, ν = 1.161).

FIGURE 10. (Contd.)

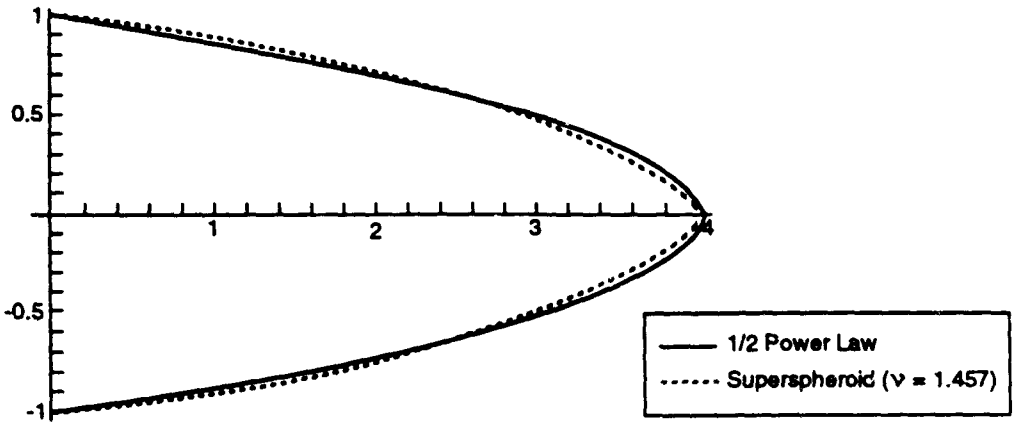

(a). One-half power law and a superpheroid (D = 2, ℓ = 4, m = 0.5; a = 4, b = 1, ν = 1.457).

FIGURE 11. Comparisons of a One-Half and a One-Quarter Power Law With a Superspheroid

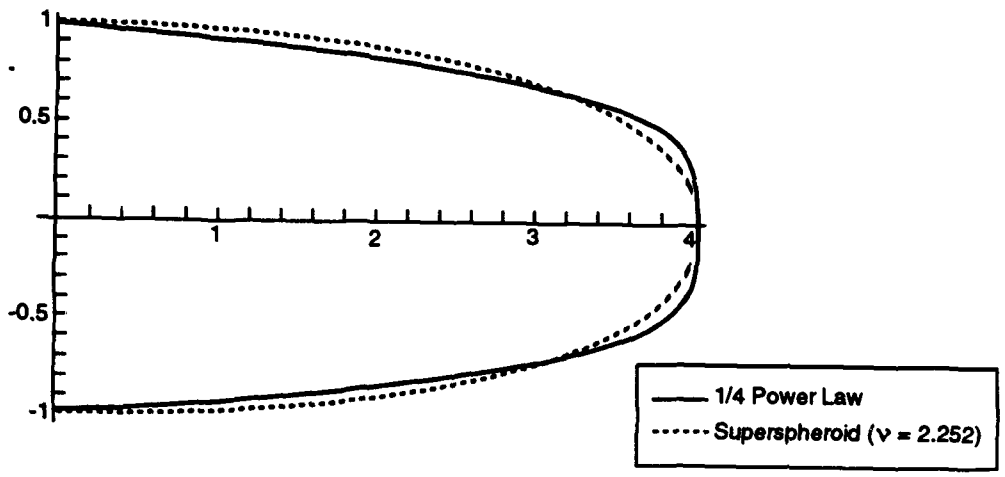

(b) One-quarter power law and a superspheroid (D = 2, ℓ = 4, m = 0.25; a = 4, b = 1, ν = 2.252).

FIGURE 11. (Contd)

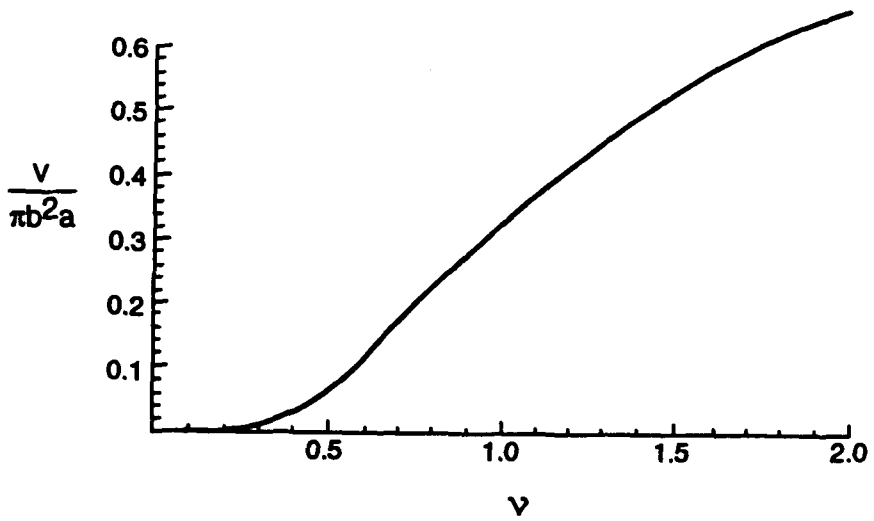

(a) Small values of ν.

FIGURE 12. Normalized Superspheroid Volume Versus ν for Small and Large Values of ν.

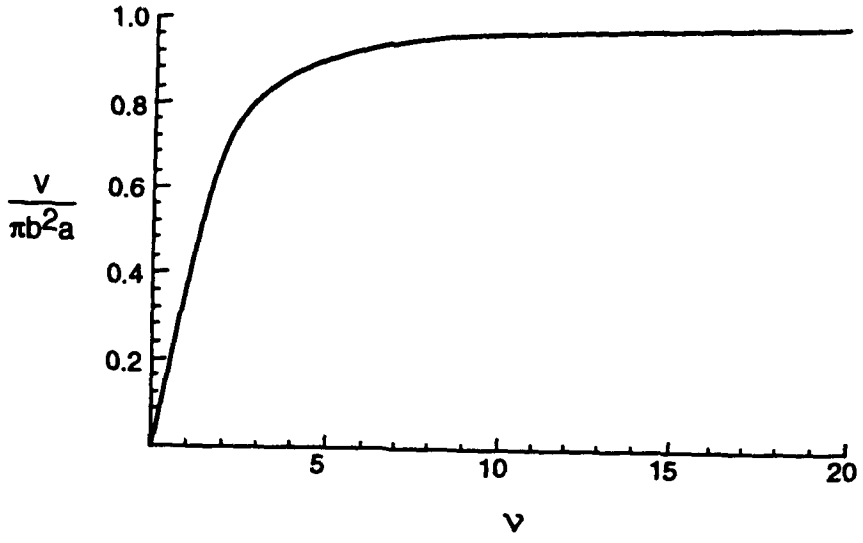

(b). Large ν.

FIGURE 12. (Contd.)

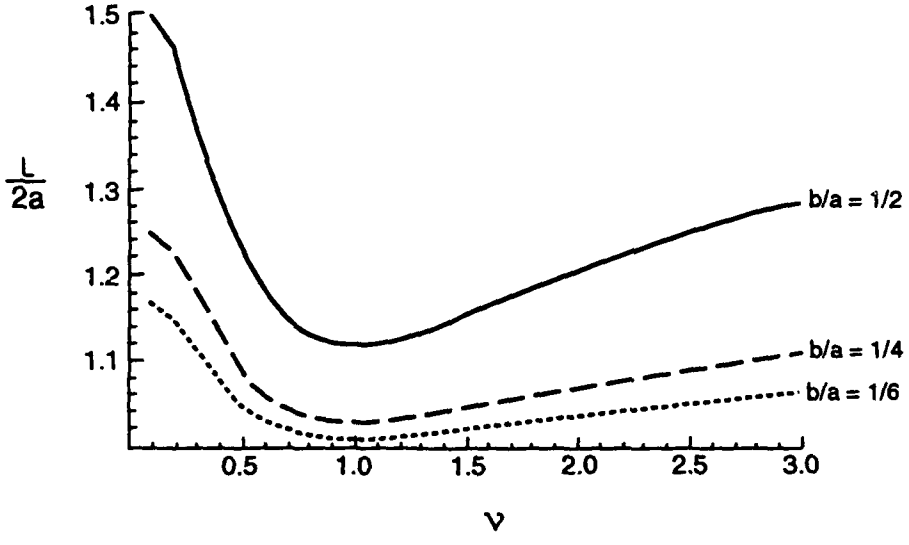

FIGURE 13. Normalized Superspheroid Arc Length (in xy Plane) Versus ν for $\frac{a}{2b}$ = 1, 2, 3.

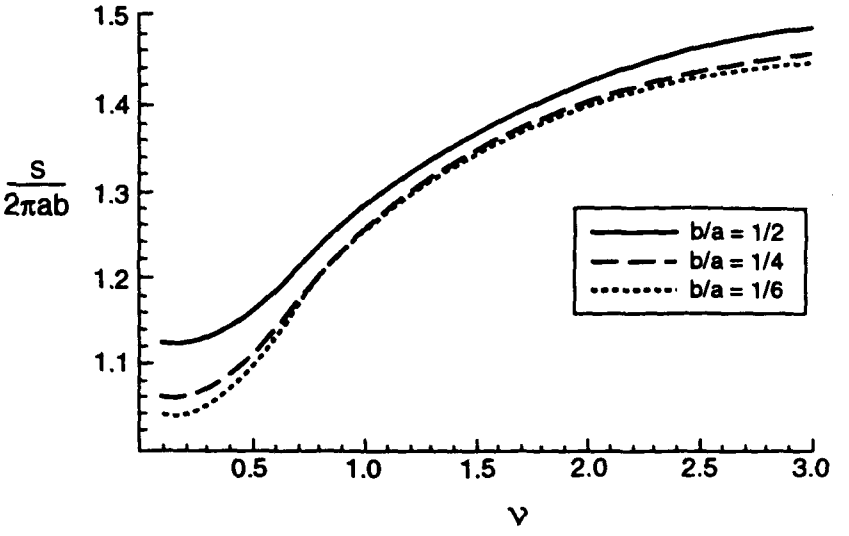

FIGURE 14. Normalized Superspheroid Lateral Surface Area Versus ν for $\frac{a}{2b} = 1, 2, 3$.

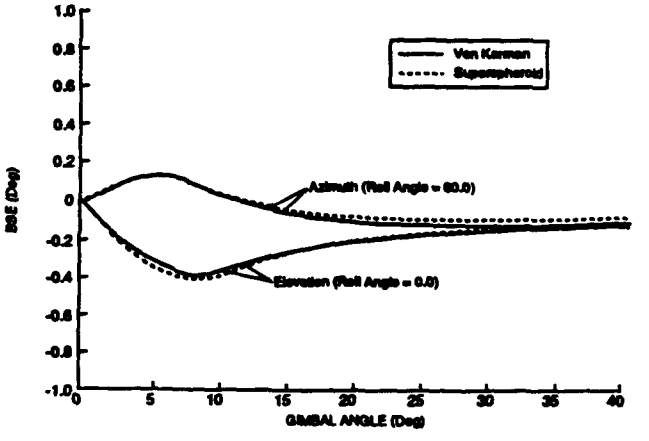

(a) BSE

FIGURE 15. Comparison of Von Karman Shape and its Optimized Superspheroid Approximation in Elevation and Azimuth on (a) BSE, (b) BSES, (c) Power Transmission.

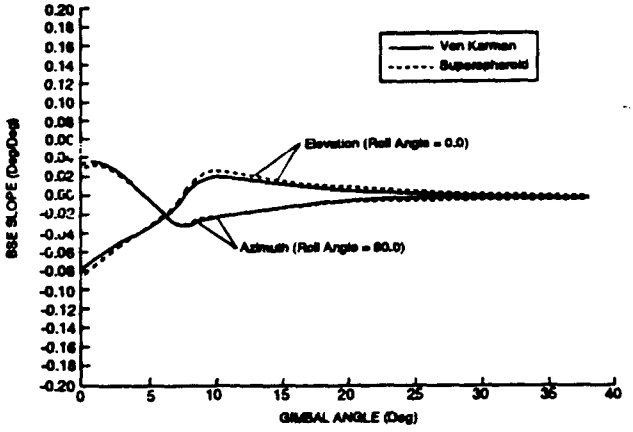

(b) BSES

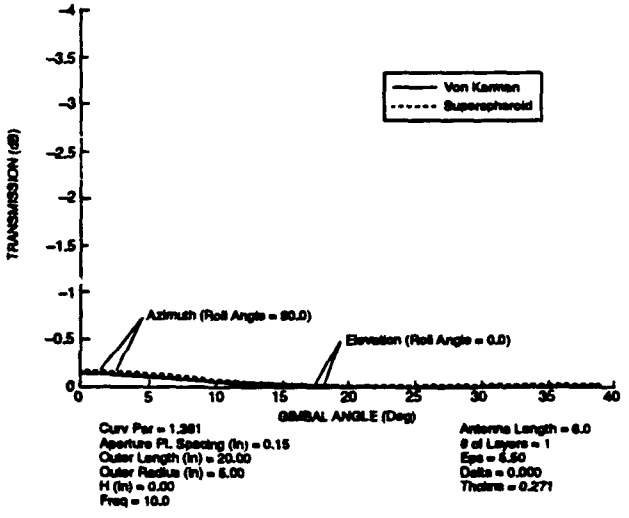

(c) Power transmission

FIGURE 15. (Contd.)

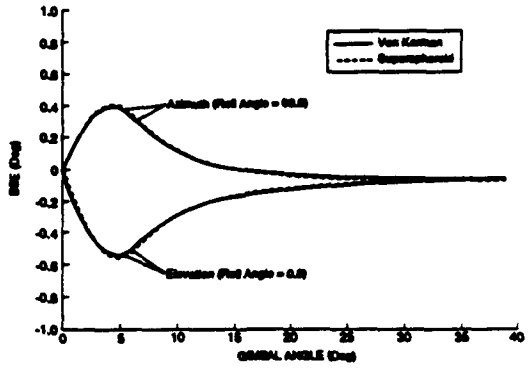

(a) BSE

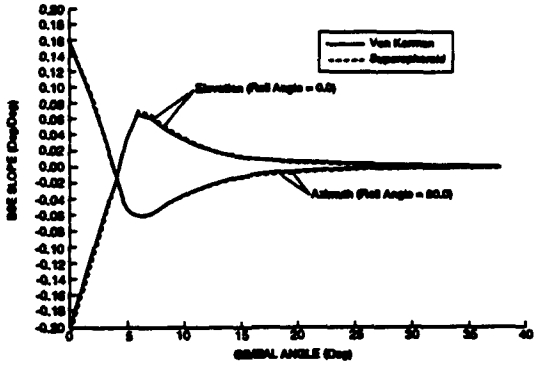

(b) BSES

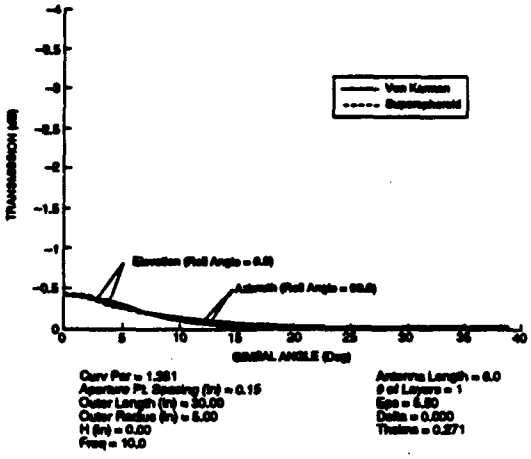

(c) Power transmission

FIGURE 16. Effect of Increasing Fineness Ratio (to 3-1) for Von Karman/Superspheroid Approximation on (a) BSE, (b), BSES, (c) Power Transmission.

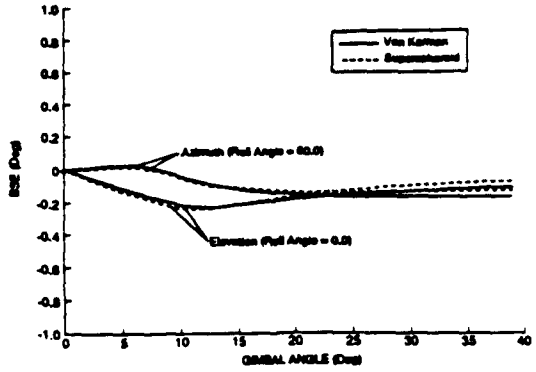

(a) BSE

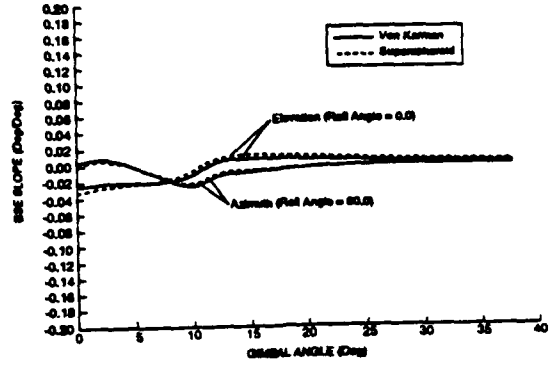

(b) BSES

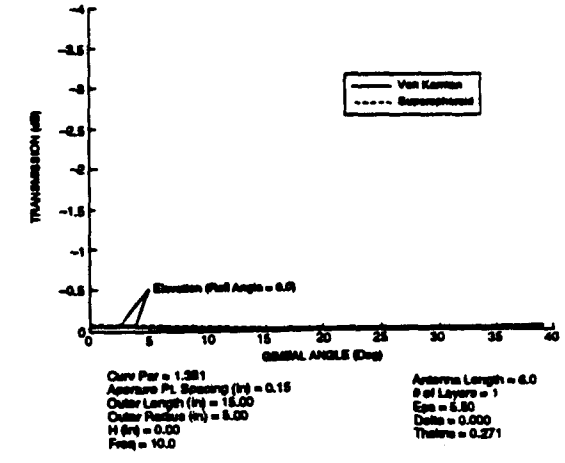

(c) Power transmission

FIGURE 17. Effect of Decreasing Fineness Ratio (to 1.5-1.0) for Von Karman/Superspheroid Approximation on (a) BSE, (b) BSES, (c) Power Transmission.

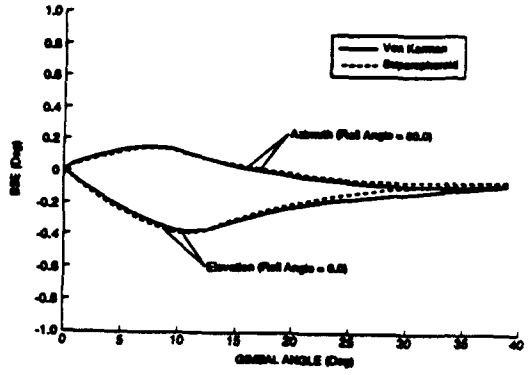

(a) BSE

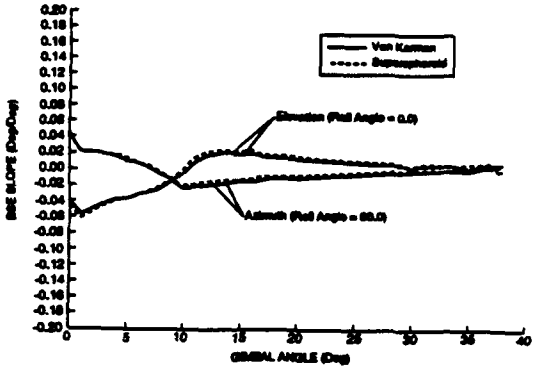

(b) BSES

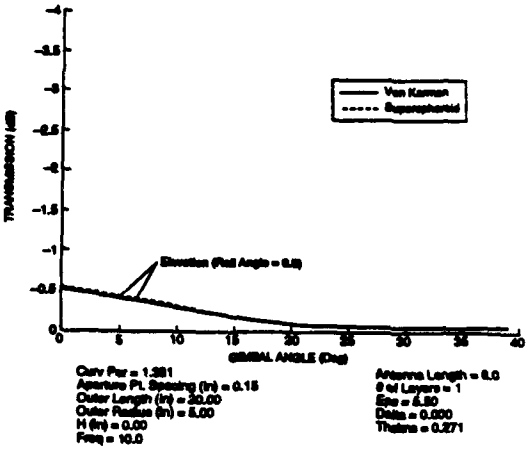

(c) Power transmission

FIGURE 18. Effect of Increasing Antenna Aperture Size for Von Karman/Superspheroid Approximation on (a) BSE, (b) BSES, (c) Power Transmission.

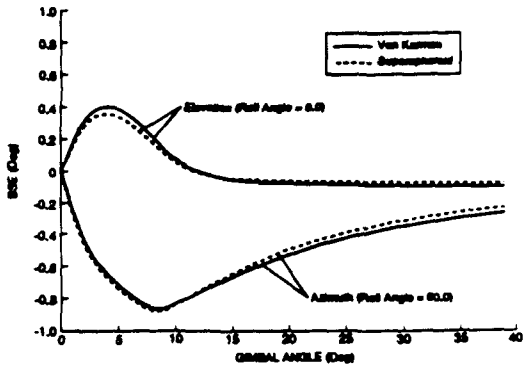

(a) BSE

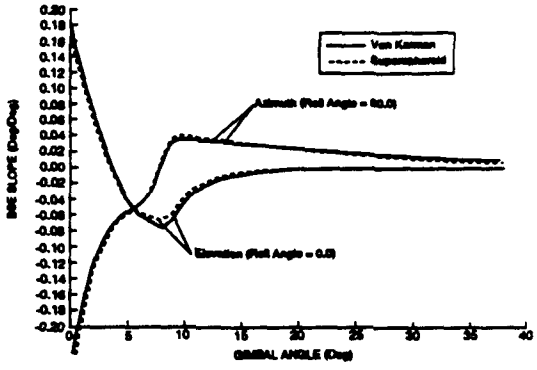

(b) BSES

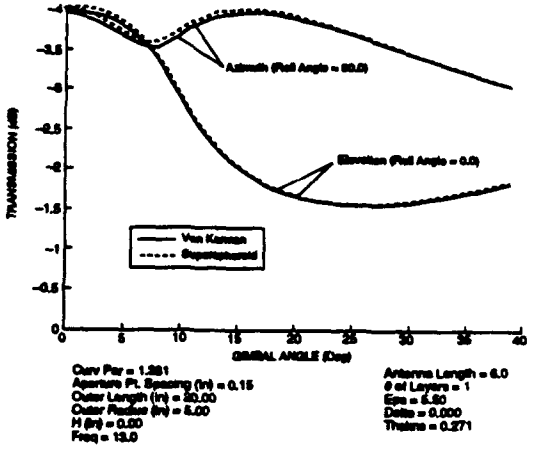

(c) Power transmission

FIGURE 19. Effect of Increasing Frequency for Von Karman/Superspheroid Approximation on (a) BSE, (b) BSES, (c) Power Transmission.

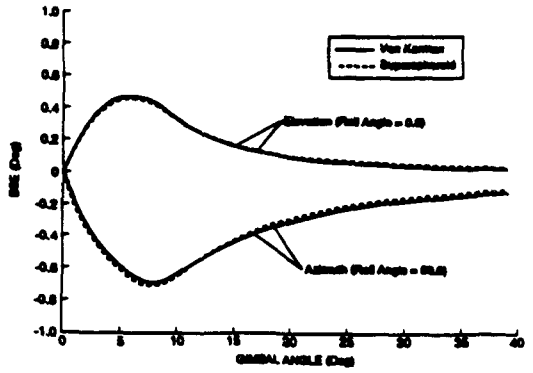

(a) BSE

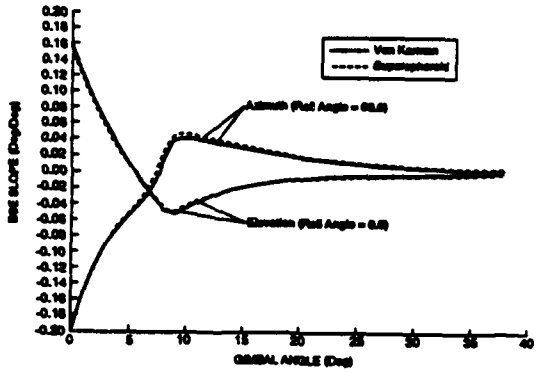

(b) BSES

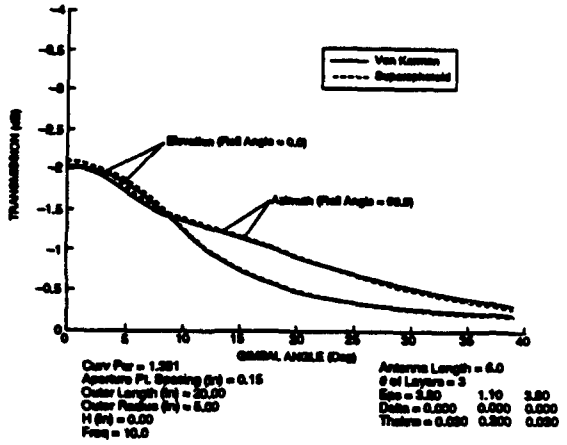

(c) Power transmission

FIGURE 20. Effect of Multiple Layers for Von Karman/Superspheroid Approximation (a) BSE, (b) BSES, (c) Power Transmission.

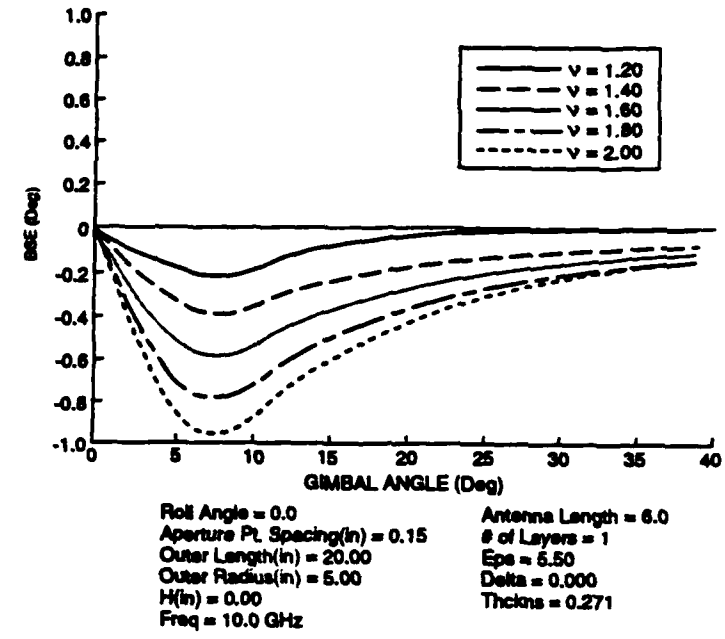

(a) Elevation

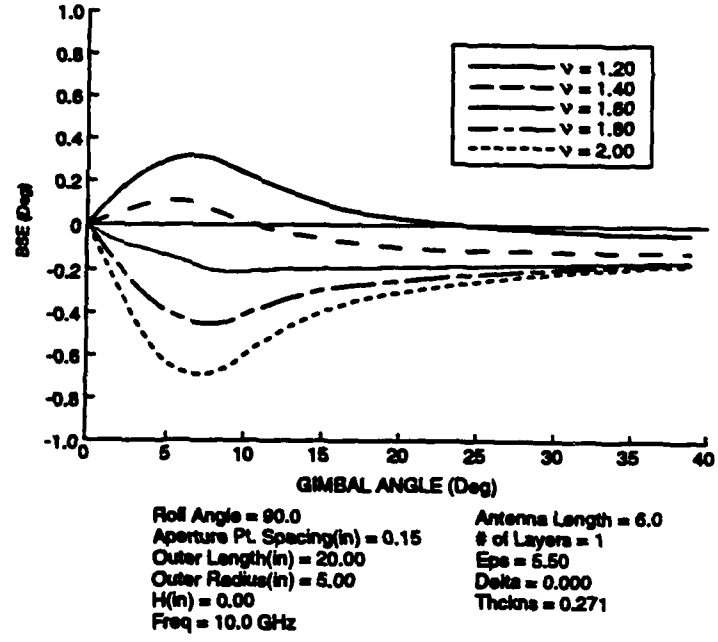

(b) Azimuth

FIGURE 21. Elevation and Azimuth BSE Versus Gimbal Angle for 2-1 Superspheroid Contours ($1.2 \leq \nu \leq 2$).

VII. REFERENCES

1. A. H. Barr. "Superquadrics and Angle Preserving Transformations," *IEEE Computer Graphics and Applications* , 1 (January 1981), pp. 11-23.

2. E. D. Constantinides and R. J. Marhefka. "Plane Wave Scattering From 2-D Perfectly Conducting Superquadric Cylinders," *IEEE Trans. Antennas Propag.*, AP-39 (March 1991), pp. 367-376.

3. D. W. Duan and Y. Rahmat-Samii. "Reflector Antennas With Superquadric Aperture Boundaries," *IEEE Trans. Antennas Propag.*, AP-41 (August 1993), pp. 1164-1167.

4. P. L. Overfelt. "Superspheroids: A New Family of Radome Shapes," to be published in *IEEE Trans. Antennas Propag.* (1994).

5. General Dynamics Corporation. *IR/RF Dome Technology Report, Vol. III, Appendices*, November 1992. (GD Report WL/MN-TR-91-46, publication UNCLASSIFIED.)

6. Air Force Weapons Laboratory. *Techniques for Airborne Radome Design, Vols. I and II*, T. E. Tice and J. D. Walton, eds., Albuquerque, N. Mex., AFWL, December 1966. (AFWL Technical Report AFAL-TR-66-391, publication UNCLASSIFIED.)

7. Naval Weapons Center. *Computer Codes for Electromagnetic Design and Analysis of Radomes*, by P. L. Overfelt. China Lake, Calif., NWC, March 1985. (NWC TP 6598, publication UNCLASSIFIED.)

8. Naval Air Warfare Center Weapons Division. *Radome Analysis and Design Tool (Final Report)*, by P. L. Overfelt, C. S. Kenney, D. J. White, and W. O. Alltop. China Lake, Calif., NAWCWPNS, November 1993. (NAWCWPNS TP 8171, publication UNCLASSIFIED.)

9. P. L. Overfelt. "Two-Dimensional Radome Modelling: A Boundary Perturbation Approach," presented at the *1984 IEEE Intl. Symposium on Antennas Propag.* (1984 IEEE Intl. Symposium Digest on Antennas Propag., June 1984. Pp. 201-205. Paper UNCLASSIFIED.)

10. P. L. Overfelt and D. J. White. "Electromagnetic Analysis of Radomes Using a Spherical Wave Point Dipole Source Array Technique," presented at the *21st Symposium on Electromagnetic Windows* (21st Symposium on Electromagnetic Windows Digest, September 1988. Pp. 11-25. Paper UNCLASSIFIED.)

11. D. C. F. Wu and R. C. Ruddock. "Plane Wave Spectrum-Surface Integration Technique for Radome Analysis," *IEEE Trans. Antennas Propag.*, AP-22 (May 1974), pp. 497-500 .

12. K. Siwiak, T. B. Dowling, and L. Lewis. "Boresight Errors Induced by Missile Radomes," *IEEE Trans. Antennas Propag.*, AP-27 (November 1979), pp. 832-841.

13. J. H. Chang and K.-K. Chan. "Analysis of a Two-Dimensional Radome of Arbitrarily Curved Surface," *IEEE Trans. Antennas Propag.*, AP-38 (October 1990), pp. 1565-1568 .

14. X. J. Gao and L. B. Felsen, "Complex Ray Analysis of Beam Transmission Through Two-Dimensional Radomes," *IEEE Trans. Antennas Propag.*, AP-33 (September 1985), pp. 963-975 .

15. C. T. Tai. *Generalized Vector and Dyadic Analysis.* New York, IEEE Press, 1992.

16. D. J. Struik. *Differential Geometry* . Cambridge, MA, Addison-Wesley, 1950.

17. A. G. Hansen. *Similarity Analyses of Boundary Value Problems in Engineering*, Englewood Cliffs, NJ, Prentice-Hall, 1964.

18. J. M. H. Olmsted. *Advanced Calculus*, New York, Crofts, Appleton, Century, 1961, Chap. 16.

19. M. Becker. *The Principles and Applications of Variational Methods*, Cambridge, MA, MIT Press, 1964, Chap. 3.

20. J. Spanier and K. B. Oldham. *An Atlas of Functions*, New York, Hemisphere, 1987, Chap 61.

INITIAL DISTRIBUTION

1 Naval Sea Systems Command, Arlington (PEO(TAD)-D26, CDR J. R. Costa)
1 Commander in Chief, U. S. Pacific Fleet, Pearl Harbor (Code 325)
1 Commander, Third Fleet
1 Commander, Seventh Fleet
2 Naval Air Warfare Center Weapons Division, Point Mugu
  Code PO3911, T. Finsod (1)
  Code PO3912, M. Zvada (1)
1 Naval Surface Warfare Center, Dahlgren Division, Dahlgren (B. Finn)
1 Naval Surface Warfare Center, Dahlgren Division, White Oak Detachment, Silver Spring
  F. Rucky (1)
  W. T. Messick (1)
1 Naval War College, Newport
1 Headquarters 497 IG INT, Falls Church (OUWG Chairman)
2 Defense Technical Information Center, Alexandria
1 Center for Naval Analyses, Alexandria, VA (Technical Library)
1 COMARCO, Incorporated, Ridgecrest, CA (D. White)
1 Georgia Institute of Technology, Atlanta, GA (E. Joy)
2 Hughes Missile Systems Company/Pomona, Pomona, CA
  B. Salmond (1)
  T. Shew (1)
1 Lindsay Associates, Carbondale, IL (J. Lindsay)
1 Lockheed Aircraft Service Company, Ontario, CA (D. Hudson)
1 Lockheed Missiles and Space Company, Incorporated, Sunnyvale, CA (J. Battles)
1 Martin-Marietta Aerospace, Orlando, FL (K. Huddleston)
1 Massachusetts Institute of Technology, Lincoln Laboratory, Lexington, MA (J. Schonfeld)
1 Texas Instruments, Incorporated, Dallas, TX (D. Purinton)
2 The Johns Hopkins University, Applied Physics Laboratory, Laurel, MD
  R. Witte (1)
  D. Yost (1)

ON-SITE DISTRIBUTION

1 Code C02
4 Code C022 (3 plus Archives Copy)
1 Code C023
2 Code C02307
    B. Alltop (1)
    C. Kenney (1)
1 Code C0231, S. Chesnut
1 Code C02313, H. Brooks
10 Code 02314, Overfelt
1 Code C0253, B. Bailey
1 Code C25233, J. Walters
1 Code C27
1 Code C2892, F. Mansfield
3 Code C2893
    G. Jaeger (1)
    W. Jaul (1)
    R. Kelley (1)
1 Code C29
1 Code C29A
4 Code C29A12
    G. Auger (1)
    R. Beyer (1)
    A. Hickle (1)
    N. Woodall (1)
1 Code C29B
2 Code C29B1
    Kartzmark (1)
    Lindsey (1)
1 Code C29B2
1 Code C29B7
2 Code C29B8
    Klissus (1)
    Nelepovitz (1)
1 Code C29B9
2 Code C2901A
    Burdick (1)
    B. Webster (1)
1 Code C2903, Baer
2 Code C29103
    G. Hewer (1)
    B. Smith (1)
1 Code C295, J. McCalester
4 Code C2951
    J. Butterworth (1)
    D. Paolino (1)
    F. Shieffen (1)
    H. Wang (1)
1 Code 29513, M. Fortune
2 Code C2952
    Ghaleb (1)
    Johansen (1)